ADVANCED FUNCTIONAL MATERIALS
www.afm-journal.de

Swimmable Micro-Battery for Targeted Power Delivery

Pengzhou Li, Zhe Yang, Chuanfa Li, Jiaxin Li, Chuang Wang, Jiawei Chen, Sijia Yu, Yanan Zhang, Yi Jiang, Yue Gao, Bingjie Wang, and Huisheng Peng**

The boom of microelectronic devices and their diverse applications has heightened the demand for innovative and effective energy supply strategies. The longevity of contemporary microelectronic devices predominantly depends on direct human intervention power supply methods, encompassing battery replacement or recharging. However, these methods may falter in specific scenarios, such as when facing liquid conditions in vivo. Here, a concept of swimmable micro-batteries (MBs) for targeted power delivery is presented. This is achieved through the design of a flexible polydimethylsiloxane/Fe_3O_4 soft-magnetic substrate for actuation, polydimethylsiloxane/neodymium-iron-boron (NdFeB) hard-magnetic tabs for precise targeting, and quasi-solid-state Zn//MnO_2 battery for power generation. These swimmable MBs exhibit an impressive areal capacity of 102.3 μAh cm-2, remarkable waterproofing, adjustable output voltage or capacity, rapid response, and accurate remote magnetic field manipulation, enabling targeted power supply available. This novel swimmable MB design broadens the function of MBs and may open a new avenue for their future development.

1. Introduction

The rise of the Internet of Things (IoT) and smart healthcare has driven the need for miniaturization and integration of electronic devices.[1–3] The increasing complexity of functions and prolonged operational requirements of microelectronic devices set higher standards for their indispensable energy supply components (e.g., batteries, capacitors, and fuel cells).[4,5] Among various energy storage devices, rechargeable aqueous MBs have gained widespread attention as promising power solutions for wearable and implantable applications due to their reliable safety, easy operating conditions, and stable voltage output.[6–10] Nevertheless, the current applications of MBs primarily confine their use to serving as single energy storage components integrated into microelectronic systems.

Ensuring a stable and uninterrupted energy supply is critical for the normal operation of electronic devices. Traditionally, people have relied on replacing or recharging batteries through direct human intervention to extend the service life of electronic devices as their power depletes. However, this approach of singular and manual energy provisioning can prove ineffective in certain scenarios, such as intricate environments in vivo,[11] where conventional bulky chargers or direct human involvement are unfeasible. For example, electrical stimulation devices in vivo still rely on surgical battery removal for replacement,[12,13] a complex procedure that results in inevitable secondary trauma and potential infection risks to the patients.[14] Consequently, in these circumstances, recharging through conventional means becomes challenging once the energy is exhausted. This scenario could lead to microelectronic devices ceasing operation and significantly shorten their overall service span.[15,16] While contemporary research on MBs mainly focuses on enhancing the electrochemical performance of individual devices and developing advanced processing or fabrication methods,[17–19] batteries are often regarded as isolated single-function energy storage units. Nonetheless, limited attention has been directed towards MBs capable of autonomously powering microelectronic devices in intricate application scenarios. It is crucial while challenging to develop a contactless power delivery strategy using MBs to meet the requirements of potential autonomous and targeted power supply scenarios.

Here, we have, for the first time, proposed and successfully validated the concept of swimmable MBs for targeted power delivery. This functional MB, capable of autonomously and contactlessly powering electronic devices, is achieved through reasonable material selection and structural design. It incorporates a flexible soft-magnetic composite substrate for actuating, hard-magnetic composite tabs for targeting, and a flexible quasi-solid-state aqueous battery for powering (**Figure 1**). Through a scalable spray printing technique, we achieve rapid and large-scale preparation of customized MBs with high throughput, adjustable voltages or capacities, and considerable electrochemical performances (e.g., high areal capacity of 102.3 μAh cm^{-2} and energy density of 141.9 μWh cm^{-2} at 10 μA cm^{-2}). The soft-magnetic polydimethylsiloxane/Fe_3O_4 (PDMS/Fe_3O_4)

P. Li, Z. Yang, C. Li, J. Li, C. Wang, J. Chen, S. Yu, Y. Zhang, Y. Jiang, Y. Gao, B. Wang, H. Peng
State Key Laboratory of Molecular Engineering of Polymers
Department of Macromolecular Science
Institute of Fiber Materials and Devices
and Laboratory of Advanced Materials
Fudan University
Shanghai 200438, China
E-mail: wangbingjie@fudan.edu.cn; penghs@fudan.edu.cn

The ORCID identification number(s) for the author(s) of this article can be found under https://doi.org/10.1002/adfm.202312188

DOI: 10.1002/adfm.202312188

Figure 1. Schematic diagram of the swimmable MB for targeted power delivery, comprising a soft-magnetic matrix for actuating, hard-magnetic tabs for targeting, and a quasi-solid-state battery for powering.

flexible substrate and hard-magnetic polydimethylsiloxane/NdFeB (PDMS/NdFeB) composite tabs enable highly controllable swimming performance, rapid responsiveness (completing a rotation cycle within 360 ms), and the capability for targeted power provisioning. These features make our swimmable MBs suitable for various applications, including navigation/transportation and targeted power delivery. Moreover, we envision the prospect of a self-powered swimmable micro-integrated system for promising applications in vivo. The conception of this functionalized swimmable MB designed for targeted power delivery not only provides new insights into MB design but also creates new possibilities for their utilization across a broad spectrum of scenarios.

2. Results and Discussion

The swimmable MBs were realized by incorporating soft-magnetic Fe_3O_4 nanoparticles (≈14 nm in diameter) and hard-magnetic NdFeB particles (≈3.6 μm in diameter) into the PDMS polymer and rolling planar Zn//MnO_2 batteries (Figures S1 and S2, Supporting Information). This ingenious structural and material design resulted in a flexible PDMS/Fe_3O_4 soft-magnetic composite substrate for actuating, PDMS/NdFeB hard-magnetic composite tabs for targeting, and a quasi-solid-state Zn//MnO_2 battery for powering (**Figure** 2a). The PDMS/NdFeB composite tabs were magnetized to saturation using an impulse magnetic field (with H ≈ 3 T) and coated with conductive silver glue to establish a stable electric connection between MBs and microelectronic devices, which led to a robust residual magnetization of 51.7 emu g^{-1} (Figure S3, Supporting Information).

Both the soft-magnetic Fe_3O_4 and hard-magnetic NdFeB can generate induced magnetization when exposed to an external magnetic field.[20] Soft-magnetic materials, such as Fe_3O_4, possess a sharp and narrow hysteresis loop due to their low coercivity (H_c), and they lose their induced magnetization upon the removal of external magnetic fields. In contrast, hard-magnetic materials like NdFeB, characterized by higher coercivity, retained high residual magnetization (M_r) against external magnetic fields once they were magnetically saturated (Figure S4, Supporting Information). By magnetizing the PDMS/NdFeB composite using an impulse magnetic field, the initially disordered NdFeB magnetic polarities embedded in PDMS resin aligned along the magnetic field direction, resulting in a macro-level permanent magnetism (Figure S5a, Supporting Information). The PDMS/NdFeB composite exhibited permanent magnetism after magnetization, demonstrated by its capability to attract numerous paper clips (Video S1, Supporting Information). In contrast, the soft-magnetic Fe_3O_4 nanoparticles embedded in the flexible PDMS substrate (Figure S6, Supporting Information) did not retain permanent magnetism. They responded to the external magnetic field by transiently aligning their magnetization but lost their magnetism instantly once the magnetic field was removed (Figure S5b, Supporting Information). Additionally, both PDMS/NdFeB and PDMS/Fe_3O_4 composites displayed considerable mechanical properties with tensile strengths of 2.0 and 0.7 MPa, respectively (Figure S7, Supporting

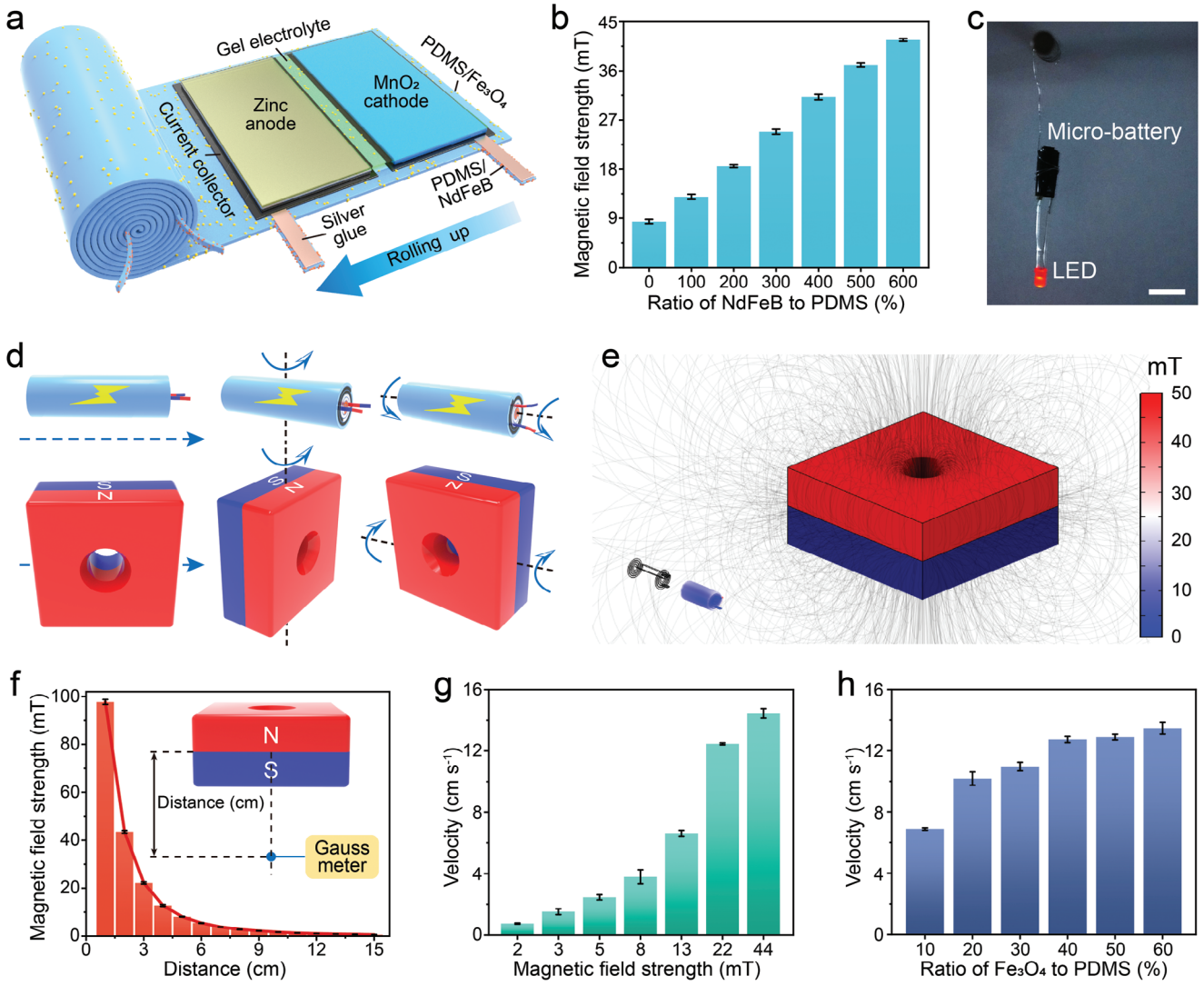

Figure 2. Characterization of the targeting and swimming performances. a) Schematic of the swimmable MB at rolled-up and planar states. b) Dependence of the magnetic field strength on the mass ratio of NdFeB to PDMS. c) Photograph of the MB hanging vertically and powering a red light-emitting dioxide. Scale bar, 5 mm. d) Demonstration of the translation, rotation, and scrolling modes of swimmable MBs manipulated by an external cubic magnetic field. e) The magnetic flux density distribution and translation mode of the MB in magnetic fields of a cuboid permanent magnet. f–h) Dependence of (f) the magnetic field strength on distance, g) the swimming velocity on magnetic field strength, and h) the swimming velocity on the mass ratio of Fe_3O_4 to PDMS.

Information). This enabled them to withstand various complex deformations during battery fabrication. The flexibility of the PDMS-based polymer substrate, combined with the utilization of metal-free carbon-based electrodes, facilitated the rolling up of planar MBs to reduce their spatial footprint. This novel "Swiss roll" configuration is expected to achieve higher volumetric energy density while maintaining a compact size (Table S1, Supporting Information).[21] Optical and scanning electron microscopic (SEM) images revealed that the swimmable MB comprised a cylindrical matrix and two "antennae-like" tabs, with the cross-section at a rolled-up state exhibiting a helical structure (Figure S8, Supporting Information).

The rational design of the soft-magnetic composite substrate and hard-magnetic composite tabs is crucial for the MB to achieve the desired swimming and targeting feature. Only when the substrate is a soft-magnetic composite and the tabs are hard-magnetic composites can the MB exhibit both swimming and targeting functionalities (Figure S9, Supporting Information). Tabs with magnetic field orientations along the thickness and radial directions can be achieved by altering the orientation of samples with respect to the magnetic field during magnetization. In this case, a radially oriented magnetic field distribution was employed to ensure the correct connection of the positive and negative electrodes when they were attracted through the North (N) and South (S) poles of the tabs in swimmable MBs (Figure S10, Supporting Information). The magnetic force of the hard-magnetic tabs can be readily regulated by adjusting the NdFeB content within the tabs. As the proportion of NdFeB increased, the magnetic field intensity of the hard-magnetic PDMS/NdFeB composite tabs increased linearly after magnetization and gradually became rigid

(Figure 2b). Notably, the tab with a mass ratio of 4:1 between NdFeB and PDMS exhibited a high magnetic field intensity of 312.5 Gs (or 31.25 mT) after magnetization (Figure S11, Supporting Information). Due to the strong magnetic field intensity of the magnetic composite, the rolled-up MB can securely attach to and stably power a vertically suspended light-emitting dioxide (LED) without any fixed measures (Figure 2c).

The dynamic magnetic fields required for remote actuation of the MBs are generated by a cuboid permanent magnet,[22,23] which can be easily manipulated and used for both magnetic torque and force on the swimmable MBs (Figures S12 and S13, Supporting Information). The magnetic torque induces rotation and alignment of the MBs along the magnetic field, while the magnetic field gradient generates a propelling magnetic force that drives the MBs forward.[24] This interplay of effects enabled the MB to undergo translation, rotation, and tumbling by adjusting the external cuboid permanent magnet accordingly (Figure 2d). Finite element analysis indicated that the MB uniformly embedded with Fe_3O_4 nanoparticles maintained an even magnetic density distribution during operation with the external cuboid permanent magnet, ensuring stable motion states during swimming (Figure 2e). By manipulating the position or orientation of the cuboid permanent magnet, the magnetic field strength around the MB can be effectively modulated. According to the Gaussian meter, the magnetic field strength applied to MBs showed a gradient change with distance, thereby allowing for the control of the swimming velocity by altering the distance between the MBs and the cuboid permanent magnet (Figure 2f). For instance, with a distance of 30 mm between the magnet's center and the MB, the resulting magnetic field strength and average swimming velocity can reach 22 mT and 12 cm s^{-1}, respectively (Figure 2g). Furthermore, maintaining a constant 10 mm distance between the external magnet and MB permitted flexible adjustment of swimming velocity by changing the Fe_3O_4 to PDMS mass ratio (Figure 2h). Unless otherwise specified, the mass ratio of Fe_3O_4 to PDMS was set at 3:10. The mobility of the swimmable MBs can be precisely controlled by rotating and dragging the cuboid magnet. Facilitated by a dynamic external magnetic field, the MBs can be directed to rotate and move by exploiting magnetic torque and force, resulting in responsive and swift motion (Video S2, Supporting Information). This non-invasive and wireless actuation method allows the swimmable MBs to move autonomously. The position images at different times indicated that the MBs can be manipulated to travel along a specific route with a stable motion state (Figure S14, Supporting Information). Driven by an external rotating magnetic field (7.5 mT, 400 rpm), the swimmable MB completed a rotation cycle within 360 ms (Figure S15, Supporting Information), demonstrating its rapid responsiveness. These results suggest the potential of combining a soft-magnetic substrate with hard-magnetic tabs as a promising strategy for creating functionally enhanced MBs with swimming and targeting capabilities.

To realize the capabilities of swimmable MBs for targeted power delivery, the aqueous, separator-free, quasi-solid-state planar Zn//MnO_2 MBs were further spray-printed due to their inherent safety, cost-effectiveness, environmental friendliness, and superior electrochemical performance (Figure S16, Supporting Information).[25,26] Prior to printing, the composition and proportions of the electrode inks were adjusted to achieve the desired rheological behavior suitable for spray printing. A noteworthy aspect was that all electrode inks exhibited characteristic shear-thinning phenomena with increasing shear rates, indicating non-Newtonian fluids (Figure S17, Supporting Information). This rheological characteristic is essential for the continuous printing of electrode inks and precise patterning of microelectrodes to prevent undesirable mixing.[27] To fabricate Zn//MnO_2 MBs, flexible, metal-free, carbon-based current collectors comprised of graphite, graphene, and conductive carbon black were initially printed onto a PDMS/Fe_3O_4 composite substrate utilizing a customized mask, followed by the accurate deposition of patterned Zn anodes and MnO_2 cathodes on each side of the current collectors. After introducing PDMS/NdFeB tabs and coating gel electrolytes, the swimmable MBs were obtained by rolling and encapsulation (Figure S18, Supporting Information). The resultant flexible electrodes demonstrated high electrical conductivities (466 S m^{-1} for Zn anode and 347 S m^{-1} for MnO_2 cathode, Figure S19, Supporting Information), attributed to the formation of continuous conductive pathways between the conductive agents and electrode materials (Figure S20, Supporting Information).[28] 2D and 3D images acquired using a step profiler indicated that the printed flexible carbon-based current collectors, Zn anodes, and MnO_2 cathodes exhibited average thicknesses of ≈11, 32, and 23 µm, respectively (Figure S21, Supporting Information). The process of spray printing offers ease of operation, flexible design capabilities, and high throughput, allowing for the creation of customizable patterns and adjustable sizes, which renders it suitable for the scalable production of MBs at high throughput.[29] Utilizing different customized masks and sequentially printing electrode inks, up to 196 MBs can be efficiently prepared on a 49 cm^2 area on various substrates like PDMS film, A4 paper, polyethylene terephthalate (PET) plates, and cloth (Figure S22, Supporting Information), demonstrating its potential for large-scale manufacturing. The printed quasi-solid-state Zn//MnO_2 MB features coplanar electrodes on a single flexible substrate with a narrow gap of 0.5 mm between the anode and cathode (Figure S23, Supporting Information), eliminating the need for separators thereby reducing the risk of short circuits.[30] This design fosters a seamless electrode-electrolyte interface, shortens ion-diffusion pathways, and provides high mechanical flexibility.

To ensure the stable and long-term operation of the MB, a modified polyvinyl alcohol (PVA)-$ZnCl_2$/$MnSO_4$-LiCl gel electrolyte was utilized by coating and solidifying in situ in ambient air. After solidification, the electrolyte retained a high ionic conductivity of 44.5 mS cm^{-1} (Figure S24, Supporting Information). The redox peaks in cyclic voltammetry curves based on the gel electrolyte displayed high similarity to the corresponding liquid electrolyte, matching well with the voltage plateaus observed in the galvanostatic charge-discharge profiles (**Figures 3**a,b). The marginally higher polarization and reduced peak current with the gel electrolyte can be attributed to its higher viscosity and comparatively lower ionic conductivity compared to the liquid electrolyte.[31,32] The overlapped cyclic voltammetry and galvanostatic charge-discharge profiles in the initial three cycles demonstrated high reversibility of the Zn^{2+} (de)intercalation reaction (Figure S25, Supporting Information). Waterproofing is a pivotal consideration for swimmable MBs given their potential operation scenarios. The planar MB, encapsulated with

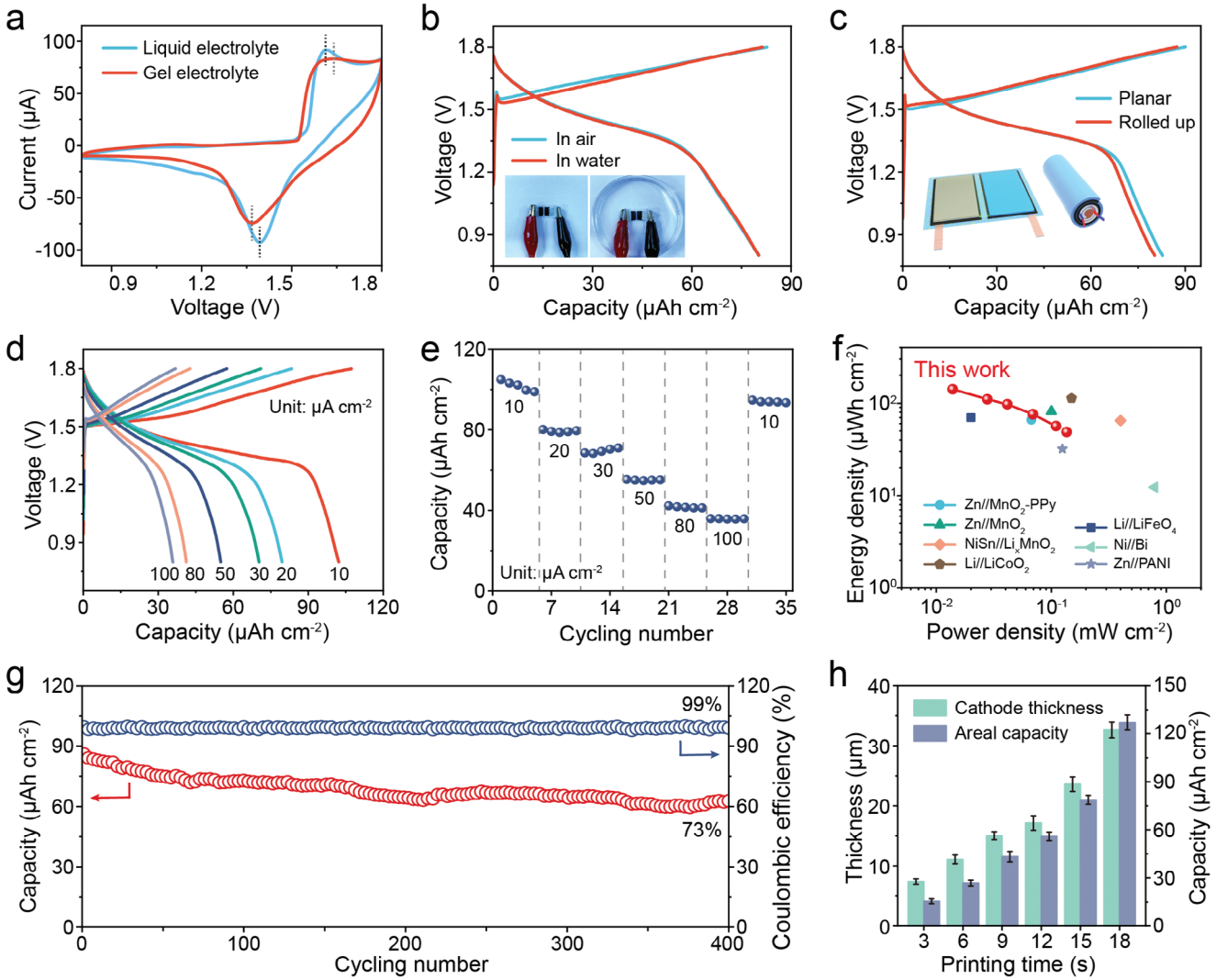

Figure 3. Electrochemical performances of the swimmable Zn//MnO_2 MB. a) Cyclic voltammetry of the MB with PVA-$ZnCl_2$/$MnSO_4$-LiCl gel electrolyte or with corresponding liquid electrolyte at a scan rate of 0.5 mV s^{-1}. b) Galvanostatic charge-discharge curves of the planar MB tested in ambient air or immersing in water. c) Galvanostatic charge-discharge curves of the MB at the planar and rolled-up states. d) Galvanostatic charge-discharge curves and e) Rate performance of the MB at increasing current densities ranging from 10 to 100 μA cm^{-2}. f) Ragone plot of the printed Zn//MnO_2 MBs in comparison to previous conventional MBs that were not swimmable. g) Cycling performance of the MB at 30 μA cm^{-2}. h) Dependence of the cathode thickness and areal capacity on the printing time of the MnO_2 cathode.

waterproof silicone rubber, demonstrated no attenuation in performance either in ambient air or when immersed in water (Figure 3b). Even after immersion in water, the MB still exhibited a high retention of 93.9% in capacity over 100 consecutive cycles at 80 μA cm^{-2} (Figure S26, Supporting Information). The fully flexible structural design, utilization of the gel electrolyte, and robust encapsulation layer contribute to the exceptional stability of the MBs under varying complex conditions (Figure S27, Supporting Information). Even when rolled into a "Swiss roll" configuration, the discharge areal capacity of the MBs showed only marginal alterations (Figure 3c). Unless otherwise specified, the "Swiss roll" MBs were fabricated and tested as follows.

Furthermore, a comprehensive characterization of the electrochemical performance of the MBs was conducted. The MBs delivered high areal capacities of 102.3, 79.6, 70.4, 55.2, and 41.3 μAh cm^{-2} at increasing current densities of 10, 20, 30, 50, and 80 μA cm^{-2}, respectively (Figure 3d). Notably, even at a high areal current density of 100 μA cm^{-2}, the MB exhibited a discharge capacity of 35.9 μAh cm^{-2}, indicating high reaction kinetics. The enhanced kinetics can be attributed to a high surface-controlled capacity contribution, accounting for up to 87.2% based on analyses of electrode reaction kinetics (Figure S28 and Note S1, Supporting Information). The capacity demonstrated an immediate recovery upon the reversal of applied current densities from 100 to 10 μA cm^{-2} across 30 cycles, demonstrating remarkable electrochemical stability (Figure 3e). Additionally, the MB achieved a notable areal energy density of 141.9 μWh cm^{-2}, surpassing many previously reported MBs (Figure 3f and Table S1, Supporting Information).[33–39] This high energy density highlights

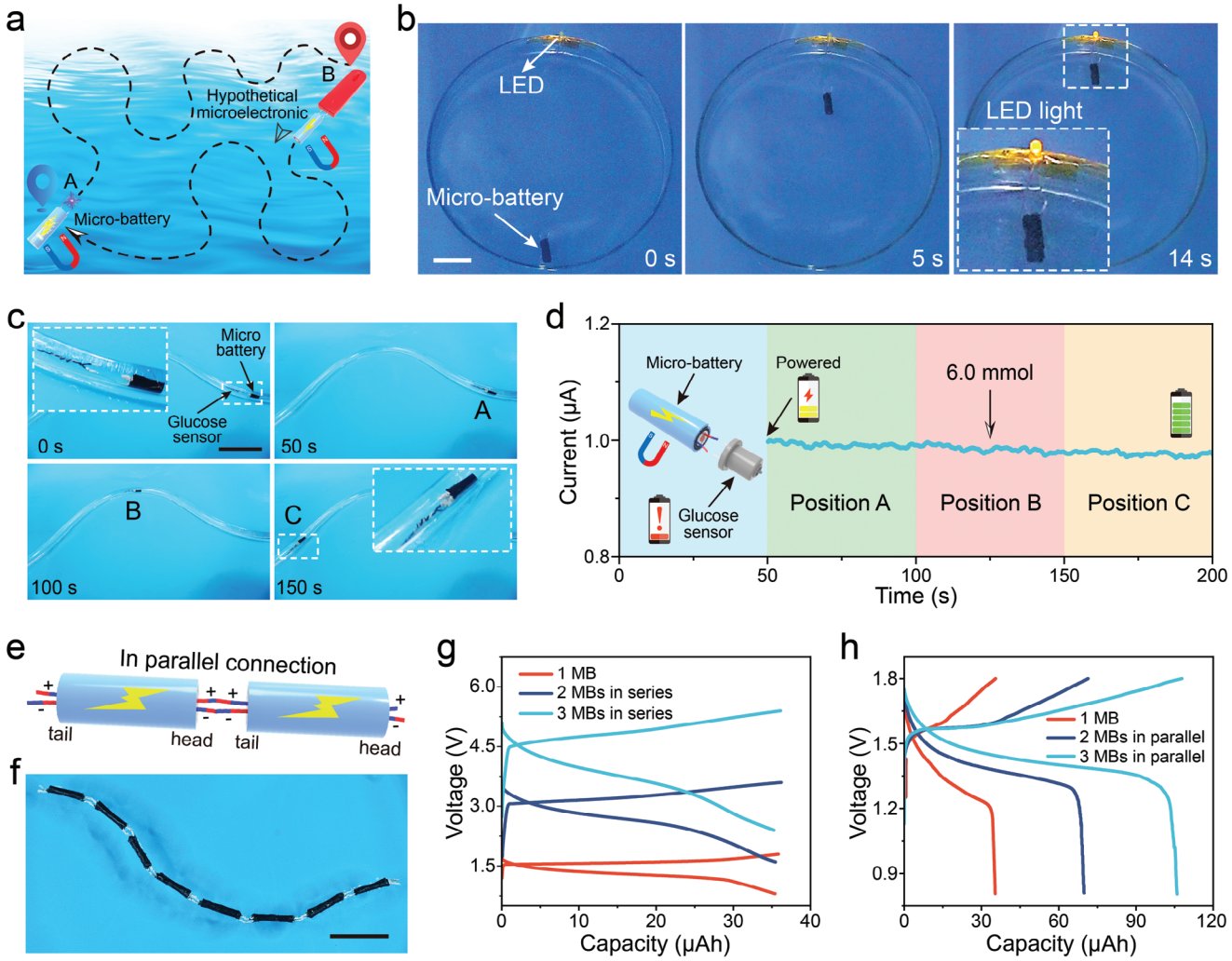

Figure 4. Application demonstrations of the swimmable MBs. a) Schematic diagram of the swimmable MB for navigation/transportation and targeted power delivery. b) Photographs of the swimmable MB powering a yellow light-emitting dioxide under the action of an external magnetic field at different times. c) Photographs of a swimmable MB powering a fiber glucose sensor at different positions. d) Response current-time curve of the fiber glucose sensor at varied positions before and after being powered by a swimmable MB. e) Schematic of the swimmable MBs connected in parallel through a "head-to-tail" connection under the control of external magnetic fields. f) Photograph of MBs connected in parallel to form a fiber-shaped battery pack. g,h) Galvanostatic charge-discharge profiles of the printed MBs connected (g) in series and (h) in parallel measured at 50 μA cm^{-2}. Scale bars, 1 cm.

its potential as a power source for commercially available implantable microelectronic devices.[40] Furthermore, the MB displayed exceptional cycling performance with 73% capacity retention and 99% Coulombic efficiency after 400 cycles at 30 μA cm^{-2} (Figure 3g). Even when operated at a higher current density of 50 μA cm^{-2} for 900 cycles, it maintained an acceptable areal capacity of 43.8 μAh cm^{-2}, accompanied by nearly 100% Coulombic efficiency (Figure S29, Supporting Information). The versatility and flexibility of spray printing allowed for convenient tailoring of the voltage and capacity of MBs during battery fabrication. By adjusting the printing time, MnO_2 cathodes with varying thicknesses and adjustable areal capacities ranging from 15.5 to 127 μAh cm^{-2} at 20 μA cm^{-2} were achieved (Figure 3h). This demonstrates the applicability of the advanced device configuration, allowing for adjustable energy demands and expanding the range of application scenarios.

The incorporation of both soft and hard magnetic composites in its design enables the swimmable MB with the capability to autonomously power electronic devices in a contactless manner, offering intriguing possibilities for diverse applications, including navigation/transportation and targeted power delivery (**Figure** 4a). For instance, when a hypothetical electronic device (red) is positioned at point A, the swimmable MB situated at point B can swiftly navigate to point A with the aid of an external magnetic field. The hard-magnetic tabs on the MB can then establish an automatic connection to the hypothetical electronic device through precise remote magnetic field control (Figure S30, Supporting Information). Subsequently, the MB efficiently dragged the electronic device back to point B, demonstrating a rapid and stable hysteresis response (Video S3, Supporting Information). Additionally, the detachment between the swimmable MB and the electronic device can be easily achieved through the control of

an external magnetic field (Figure S31 and Video S4, Supporting Information). This contactless switch control is of significant importance for the reuse and recycling of swimmable MBs. To intuitively exhibit the targeted power delivery capability, a swimmable MB can gradually approach a fixed LED under precise control of the external magnetic field. Upon contact between the MB's two "tentacle-like" hard-magnetic tabs and the LED's electrodes, the yellow LED instantaneously illuminates (Figure 4b and Video S5, Supporting Information). The strong magnetic field intensity of the hard-magnetic tabs ensured a reliable circuit connection with the LED, thus maintaining continuous brightness. It is noteworthy that the LED serves as a simplified model to demonstrate the targeted power delivery capability of our swimmable MBs, which can be extended to other microelectronic devices.

The MB's swimming capability enables uninterrupted power delivery to microelectronic devices during movement, enabling their continuous operation across different locations. As depicted in Figure 4c, when an exhausted fiber glucose sensor is positioned at point A within a simulated blood vessel (6 mm in inner diameter), a swimmable MB can provide targeted power delivery through remote manipulation of an external magnetic field. The signal data were recorded with an electrochemical workstation by connecting it in series to the MB and the fiber glucose sensor using copper wires, allowing continuous monitoring of glucose concentration (≈6.0 mmol) at point A. Subsequently, the MB guided the sensor through positions B and C, sequentially recording glucose concentrations at each location (Figures 4d). Benefitted from the use of intrinsic biocompatible materials and a safe aqueous Zn//MnO_2 battery system,[41–45] there were no signs of inflammation and immune response observed after implanting the swimmable MB in rats for one week (Figure S32, Supporting Information), indicating significant potential for applications in vivo. These results demonstrate the capability of our swimmable MBs not only to store energy but also to deliver it in a targeted manner. Additionally, MBs with different sections in series could be facilely prepared at a large scale (Figure S33, Supporting Information). And parallel-connected fiber-shaped battery packs could be assembled through "head-to-tail" connections under the control of external magnetic fields (Figures 4e,f). Irrespective of whether swimmable MBs are connected in series or parallel, they exhibit similar galvanostatic charge-discharge profiles, indicating the same electrochemical process. The MBs connected in series monotonously increased the plateau voltage with unchanged capacity (Figures 4g and Figure S34, Supporting Information), while the parallelly connected MBs maintained a stable average plateau voltage with proportional growth in discharge capacity (Figure 4h), demonstrating consistent and outstanding performance. As a demonstration, a thermometer and light-emitting diode (LED) could be powered by a single swimmable MB or by employing three sections in series (Figure S35, Supporting Information), demonstrating the inherent potential as microscale power sources.

The swimmable MBs derived from the in-plane structure are highly customizable and compatible with advanced micro/nano processing technologies (e.g., lithography, inkjet printing, thermal evaporation, and magnetron sputtering). These manufacturing methods enable easy integrations of MBs with various planar microelectronic devices, including batteries,[46] sensors,[47] transistors,[48] and displays,[49] all of which are also prepared using micro/nanofabrication techniques. This compatibility facilitates their easy integration into the fabrication of functional microelectronic integrated systems. In the future, by utilizing the "Swiss roll" configuration alongside specific soft or hard-magnetic composites, a self-powered swimmable micro-integrated system could be constructed as a multifunctional platform. This system would encompass energy harvesting (e.g., microbial fuel cells), energy storage (e.g., MBs), health monitoring (e.g., micro-sensors), signal processing (e.g., chip), signal transmission, and disease therapy (e.g., drug delivery). Such a system would realize the vision of the physician in vivo (**Figure 5**a). Compared to traditional MBs or micro-robots that serve singular functions, the swimmable micro-integrated system possesses various functionalities, making them ideal for numerous applications. For instance, they could be implanted into the body through non-invasive oral or minimally invasive injection methods.[50,51] Driven by external magnetic torque and force, they could serve as mobile "gas stations" within the body, effectively powering implantable medical microelectronic devices and considerably extending their operational lifespan. With their unique structural and material design, these swimmable micro-integrated systems could go beyond the traditional function of single devices, emerging as effective tools for life science research, physiological detection, and disease treatment (Figure 5b).

3. Conclusion

In summary, a swimmable MB for targeted power delivery has been achieved through a flexible spray printing process. This approach enables rapid and scalable production of customized MBs with adjustable voltages or capacities, alongside excellent electrochemical performance (high areal capacity of 102.3 μAh cm^{-2} and energy density of 141.9 μWh cm^{-2} at 10 μA cm^{-2}). The incorporation of a PDMS/Fe_3O_4 soft-magnetic substrate and PDMS/NdFeB hard-magnetic tabs endows the swimmable MB with rapid response (completing a rotation cycle within 360 ms), superior swimming properties, and targeted power supply capabilities under the action of an external magnetic field. Additionally, potential application scenarios have been explored and preliminary proof-of-concept demonstrations have been conducted. Finally, a self-powered swimmable micro-integrated system has been proposed with potential applications in vivo. In this study, we opted for the widely studied materials to enhance the validation of this innovative concept. Looking forward, the performance of swimmable MBs can be further enhanced by developing novel material systems, devising new actuation methods, and delving into more intricate application scenarios. The demonstration of this functionalized swimmable MB may change people's views on traditional battery function with single energy storage and provide new insights for their development.

4. Experimental Section

Materials and Reagents: Superfine graphite (≥ 99%) and N, N-dimethylformamide (DMF, ≥ 99.8%) were purchased from Adamas. Manganese sulfate monohydrate ($MnSO_4 \cdot H_2O$, ≥ 99%), graphene (3000 mesh), potassium hexachloroplatinate (K_2PtCl_6, Pt 39.6%), bovine serum albumin (BSA, ≥ 98%), and 5 wt% Nafion solution were obtained from

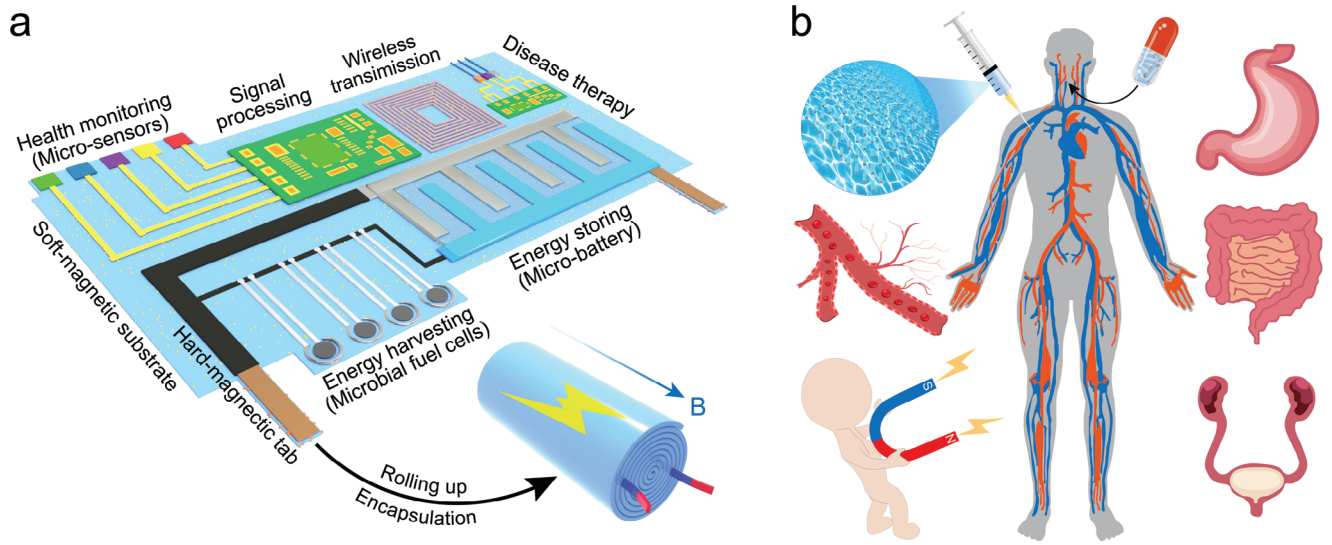

Figure 5. Perspective on swimmable MB. a) Schematic diagram of the concept of a self-powered swimmable micro-integrated system consisting of energy harvesting, energy storing, signal monitoring, signal processing, wireless transmission, and disease therapy modules. b) Illustration of the swimmable micro-integrated system for potential applications in vivo.

Sigma-Aldrich. Zinc powder (99.99%), zinc chloride ($ZnCl_2$, 98%), lithium chloride (LiCl, AR, ≥ 99%), glucose oxidase from Aspergillus niger, and glutaraldehyde (AR, 50% in H_2O) were purchased from Aladdin. Thermoplastic polyurethane (TPU, 2792A) was obtained from Covestro. Poly(vinyl alcohol) (PVA, 1799) was purchased from Macklin. Conductive carbon black (Super P, 30–45 nm) was purchased from XFNANO Material Technology Co., Ltd. Silver conductive ink was purchased from Alfa Aesar. Sodium hydroxide (NaOH, AR), iron chloride hexahydrate ($FeCl_3{\cdot}6H_2O$, AR), potassium permanganate ($KMnO_4$, AR, ≥ 99.5%), and sulfuric acid (H_2SO_4, AR) were purchased from Sinopharm Chemical Reagent Co., Ltd. Iron chloride tetrahydrate ($FeCl_2{\cdot}4H_2O$, AR) was purchased from J&K Scientific Chemical Co., Ltd. Neodymium-iron-boron bonded magnetic powder (NdFeB, LW-BA, 2000 mesh) was purchased from Guangzhou Xinnuode transmission components Co., Ltd. Lignocellulose was purchased from Shanghai Chenqi Chemical Technology Co., Ltd. Conductive silver paste (SECrosslink 4200) was purchased from Shanghai Juhe Advanced Materials Technology Co., Ltd. Polydimethylsiloxane resin (PDMS, Silicone SYLGARD 184 Elastomer Kit) was purchased from Dow Chemical Company. Silicone sealant (Kafuter, K-705) was purchased from Guangdong Hengda New Materials Technology Co., Ltd. β-D-Glucose ($C_6H_{12}O_6$, > 85%) was purchased from TCI (Shanghai) Chemical Industrial Development Co., Ltd. Paraformaldehyde fixative, hematoxylin-eosin (H&E) stain kit, 4′,6-diamidino-2-phenylindole (DAPI), anti-CD68 Rabbit pAb (GB113109), and Cy3 conjugated Goat Anti-Rabbit lgG (H+L) (GB21303) were purchased from Solarbio Science and Technology Co., Ltd. All reagents were used as received without further purification.

Synthesis of Magnetic Fe_3O_4 Nanoparticles: The magnetic Fe_3O_4 nanoparticles were synthesized via a modified co-precipitation method.[52] First, 0.254 g (0.016 mol) $FeCl_2{\cdot}4H_2O$ and 0.172 g (0.008 mol) $FeCl_3{\cdot}6H_2O$ were dissolved in 80 mL of deionized water in a 250 mL three-neck flask. The resulting mixture solution was vigorously stirred at 50 °C for 1 h under a nitrogen atmosphere. Next, 10 mL of 0.5 M NaOH solution was added dropwise into the above solution with an obvious color change from brown to black, indicating the formation of Fe_3O_4 nanoparticles. The resulting black solution was then cooled down to room temperature and continuously stirred for 1 h to allow for complete crystallization. The solution was then allowed to ultrasound agitation for 1 h and centrifuged three times with deionized water. Finally, the resulting product was dried in a vacuum oven at 50 °C for 24 h to obtain the magnetic Fe_3O_4 nanoparticles.

Synthesis of α-MnO_2 Nanorods: α-MnO_2 nanorods for cathode materials of swimmable MBs were synthesized via a modified hydrothermal method.[53,54] Specifically, a 50 mL solution was prepared by adding 0.25 g $MnSO_4$ and 1.0 mL of 0.5 M H_2SO_4 to the deionized water under vigorous stirring. Subsequently, 25 mL of 0.05 M $KMnO_4$ solution was slowly added to the above solution and continuously stirred for 8 h at room temperature. Then, the resulting solution was transferred into a Teflon-lined polytetrafluoroethylene (PTFE) autoclave vessel and heated at 120 °C for 10 h. Finally, the obtained α-MnO_2 slurry was centrifuged several times at 10 000 rpm for 10 min and dried in a vacuum oven at 80 °C for 24 h for further use.

Preparation of Electrode Inks: To prepare the electrode inks with desirable viscosity for spray-printing, a specific amount of thermoplastic polyurethane resin (TPU) was added to N, N-dimethylformamide (DMF) solvent and heated at 80 °C for 2 h to fully dissolve the resin. Then, superfine graphite, graphene, carbon black, and electrode active materials (Zn powder and α-MnO_2 powder) were added to the above resin solution with intensive stirring for 60 min to achieve the electrode inks. For carbon-based conductive ink used as flexible current collectors, the mass percentages of TPU, superfine graphite, graphene, and carbon black were 15%, 15%, 23%, and 47%, respectively. For MnO_2 cathode ink, the mass percentages of TPU, superfine graphite, graphene, carbon black, and MnO_2 powder were 6%, 6%, 9%, 19%, and 60%, respectively. For Zn anode ink, the mass percentages of TPU, superfine graphite, graphene, carbon black, and Zn powder were 8%, 4%, 6%, 12%, and 70%, respectively.

Preparation of Gel Electrolyte for Swimmable MBs: A modified PVA-$ZnCl_2$/$MnSO_4$-LiCl gel electrolyte was prepared for quasi-solid-state Zn//MnO_2 MBs.[55] Specifically, 3 M LiCl (1.27 g), 2 M $ZnCl_2$ (2.726 g), 0.4 M $MnSO_4$ (0.676 g), 0.25 g lignocellulose, and 1 g PVA were mixed in 10 mL of deionized water and heated at 90 °C for 1 h under vigorous stirring. After cooling to room temperature (25 °C), the PVA-$ZnCl_2$/$MnSO_4$-LiCl quasi-solid-state gel electrolyte was obtained for further use.

Preparation of Soft and Hard Magnetic Composites: The magnetic composite slurries were prepared by uniformly mixing NdFeB microparticles (with an average size of 3.6 µm) or Fe_3O_4 nanoparticles (with an average size of 14.2 nm) into uncured PDMS resin. Subsequently, 10 wt% of the curing agent containing platinum catalyst was added and stirred for 2 min at room temperature (25 °C). To prepare PDMS/Fe_3O_4 soft magnetic composite film, 5 mL of the corresponding mixture was dispensed onto a 10 cm^2 polyethylene terephthalate (PET) plate (with a thickness of 500 µm) and spin-coated at 1000 rpm for 60 s. This process was repeated three times, and the PDMS/Fe_3O_4 composite film was dried at 60 °C for 6 h. To prepare the PDMS/NdFeB hard-magnetic composite, the corresponding

mixture was poured into a Teflon mold with a thickness of 0.6 mm and then dried at 60 °C for 6 h. Finally, the composite film was magnetized by impulse magnetic fields (about 3 T) generated by an impulse magnetizer (IM-10-30, ASC Scientific) to impart magnetic polarities to the NdFeB particles embedded in the PDMS resin.

Preparation of Flexible Electrodes: Flexible planar interdigitated electrodes were prepared using a step-by-step spray printing technology. First, the substrate (such as PDMS, PET, and A4 paper) covered with a customized patterned mask was placed on a 60 °C hot plate. Next, carbon-based conductive ink was added to the spray gun barrel and sprayed onto the substrate through the mask. The resulting electrodes were then placed in an oven and dried at 60 °C for 30 min to remove excess solvent. After drying, the MnO_2 cathode and Zn anode were spray-printed onto the two sides of the carbon-based current collectors using the same approach successively. Finally, the flexible electrodes were obtained after being fully dried in a vacuum oven at 60 °C for 12 h.

Assembly of Swimmable MB: To assemble the swimmable MB, the magnetized PDMS/NdFeB composite was cut into strips and tightly boned with the PDMS/Fe_3O_4 composite film using commercial 502 glue. Then, the conductive silver glue was evenly coated on the surface of the PDMS/NdFeB composite film and dried at 80 °C to ensure a strong connection with the flexible MnO_2 cathode and Zn anode. Then the PVA-$ZnCl_2$/$MnSO_4$-LiCl gel electrolyte was uniformly dip-coated onto the flexible electrodes and left under ambient air at room temperature for 12 h to remove excess water. Once the surface of the gel electrolyte was solidified, the mechanically robust planar quasi-solid-state Zn//MnO_2 MB was obtained. Finally, by rolling up the planar battery and encapsulating it with waterproof silicone sealant, the swimmable MB could be obtained.

Fabrication of Fiber Glucose Sensor: The fiber glucose sensor was fabricated by twisting the glucose-sensing fiber and Ag/AgCl/carbon nanotube (CNT) fiber together,[56] with 1 µL of 10% PVA filling between the two electrodes to avoid short circuits. The sensor was tested with a two-electrode system with the glucose-sensing fiber serving as the working electrode while the Ag/AgCl/CNT fiber serving as both reference and counter electrode. First, platinum (Pt) nanoparticles were electrodeposited onto a CNT fiber to prepare the H_2O_2 sensor. The electrodeposition was performed under a pulse electrodeposition mode (0.5 V for 10 s and −0.7 V for 10 s until the charge number reached 0.02 C) in a mixed solution containing 1 mM K_2PtCl_6 and 0.1 M KCl. Next, the Pt/CNT fiber was dip-coated with 3 µL of the mixed enzyme immobilization solution containing glucose oxidase (40 mg mL^{-1}), bovine serum albumin (BSA, 40 mg mL^{-1}), and glutaraldehyde (0.15% w/w). Finally, the Pt/CNT fiber was uniformly coated with a Nafion solution (0.1 wt%, 2.5 µL) three times. To fabricate the Ag/AgCl/CNT fiber electrode, Ag was first electrodeposited onto a CNT fiber in a two-electrode system with the CNT fiber as the working electrode and a commercial silver electrode as both counter and reference electrode. The electrodeposition was performed under a cyclic voltammetry mode (with a voltage window of −0.9 to 0.9 V for 10 cycles at 0.1 V s^{-1}) containing 5 mM $AgNO_3$ and 1 M KNO_3. Then, AgCl was electrodeposited onto the obtained Ag/CNT fiber in a two-electrode system with the Ag/CNT fiber used as the working electrode while a commercial Ag/AgCl electrode served as both counter and reference electrode. The electrodeposition was also conducted under a cyclic voltammetry mode (with a voltage window of −0.15 to 1.05 V for 2 cycles at 0.05 V s^{-1}) containing a mixed solution with 0.1 M KCl and 0.01 M HCl. The Ag/AgCl reference fiber electrode could be used after drying overnight and the resulting fiber glucose sensor was stored at 4 °C before testing.

Electrochemical Measurement: Cyclic voltammetry (CV) and galvanostatic charge-discharge (GCD) profiles of the MB were carried out by using a CHI660E electrochemical workstation. Electrochemical impedance spectroscopy (EIS) was conducted from 0.1 MHz to 10 mHz with a potential amplitude of 5 mV. Galvanostatic charge-discharge profiles and cycling measurements were carried out using the LAND CT2001A battery test system (Wuhan Land Electronic Co., Ltd, China).

The ionic conductivities of the gel electrolyte were measured by sandwiching electrolytes between two stainless steel (SS) foil (1 × 1 cm) serving as blocking electrodes. The measurements were performed over a frequency range of 1 MHz to 100 mHz with 10 mV AC amplitude. The ionic conductivity (σ, $S\ cm^{-1}$) was estimated using the following equation.[57]

$$\sigma = l/\left(R_b \cdot A\right) \tag{1}$$

where l represents the distance between the two stainless steel electrodes, R_b is the ohmic resistance of the electrode, and A is the electrode area.

Characterizations: The microstructure and morphology of the materials were characterized using the transmission electron microscope (TEM, JEOL JEM-2100F operated at 200 kV) and cryo field-emission scanning electron microscopy (Zeiss FE-SEM Ultra 55 operated at 3 kV) equipped with an energy-dispersive spectrometer (EDS) detector. X-ray diffraction (XRD) patterns were recorded using a Burker-AXS with Cu-Kα_1 radiation. The magnetic field density of the PDMS/NdFeB hard-magnetic composite was measured by a Gauss meter (Shanghai Daxue Electromagnetic Equipment Co., Ltd., China). The magnetic hysteresis loops of the magnetic composite film were obtained using a vibrating sample magnetometer (VSM, Lake Shore 7410, USA). The thickness of the printed flexible electrodes was measured using an Alpha step D-600. The conductivity of the printed electrode was measured using four-point probe equipment (RTS-9). Photographs were taken with a digital camera (SONY A6000, Japan).

Manipulation: The spatially varying magnetic actuating field was generated by a commercial NdFeB permanent magnet (N42, 50 × 25 × 25 mm, Beijing Zhongke Sanhuan High Technology Co., Ltd., China, Figure S12, Supporting Information) for the manipulation of swimmable MBs. The dynamical transformations of the swimmable MBs were achieved by combining vertical, horizontal, and rotational movements of the magnet. The magnetic field intensity could be tuned by adjusting the distance between the MBs and the magnet.

Calculation: The areal capacities C_{device} (µAh cm^{-2}) of Zn//MnO_2 MBs were calculated from galvanostatic charge-discharge curves using the following equation.

$$C_{device} = It/A_{device} \tag{2}$$

where C_{device} (µAh cm^{-2}) is the areal capacity, I (µA) is the discharge current, t (h) is the discharge time, and A_{device} (cm^2) is the total electrode area.

The areal energy density and power density of Zn//MnO_2 MBs were calculated using Equations (3) and (4).

$$E_{areal} = I \int Udt/A_{device} \tag{3}$$

$$P_{areal} = \left(E_{areal}/t\right) \times 3600 \tag{4}$$

where U (V) is the voltage, E_{areal} (µWh cm^{-2}) is the areal energy density, and P_{areal} (mW cm^{-2}) is the areal power density.

Finite Element Simulation: The magnetic flux density distribution and translation mode of an MB under the magnetic field generated by a cuboid permanent magnet were simulated using finite element analysis. As shown in Figure 2e, a cuboid permanent magnet with a residual magnetization of 1000 kA m^{-1}, measuring 45 mm in length, 45 mm in width, and 20 mm in height, was used. The dimension of the MB set at 5 cm away from the surface of the permanent magnet was 0.4 cm in diameter and 1 cm in length. The material of the soft-magnetic substrate was set as 30 wt% Fe_3O_4 and 70 wt% PDMS while the hard-magnetic tabs consisted of 20 wt% NdFeB and 80 wt% PDMS. To simulate the translation of the MB, its movement was constrained in the other two directions. Free tetrahedral meshing and swept meshing were used for the MB and air domains, respectively.

Implantation of Swimmable MBs: Experimental rats (SD, male, 6–8 weeks) were purchased from Shanghai Slaughter Laboratory Animal Co. All animal experiments were conducted following the protocol approved by the Animal Experimentation Committee of Fudan University, with the approval number SYXK2020-0032. All animal handling adhered strictly to the operational requirements of the National Institutes of Health and Fudan University. After thorough preoperative cleaning, the rats were

anesthetized with 2% isoflurane and placed gently on a surgical positioning table. The swimmable MB was implanted into the leg muscle tissue of the rats using a syringe. One week after the implantation, blood samples were collected from the rats and stored at 4 °C before use. Major organs, including the heart, liver, spleen, lung, and kidney, as well as leg muscle tissues from the control and implanted rats, were excised and placed in paraformaldehyde fixative. The tissue was dehydrated using a gradient concentration of ethanol and then embedded in paraffin wax. Paraffin blocks were sliced into 6 µm thick sections and stored at room temperature.

Biocompatibility Tests: Blood cell analysis, enzyme-linked immunosorbent assay (Elisa), tissue sections, and immunofluorescence staining experiments were conducted to verify the biocompatibility of swimmable MBs. For blood cell analysis, blood samples collected from the rats were tested using a veterinary fully automatic blood cell analyzer (Mindray, BC-5000vet). Typical inflammatory-related markers, including white blood cell (WBC), neutrophil (Neu), lymphocyte (Lym), monocyte (Mono), eosinophils (Eos), and basophils (Bas), were analyzed. For enzyme-linked immunosorbent assay (Elisa), serum was obtained by centrifuging the blood sample at 3000 rpm for 10 min. Concentrations of interleukin-1β (IL-1β), interleukin-6 (IL-6), and tumor necrosis factor-α (TNF-α) were measured using enzyme-linked immunosorbent assay kits (Wuhan Service Biotechnology CO., LTD). For H&E staining, the tissue slices were processed with xylene, anhydrous ethanol, 75% ethanol, and water. Hematoxylin staining involved immersing the slices for 3–5 min in differentiation solution, reblue solution, and hematoxylin staining solutions, respectively. Following this, the slices were re-dehydrated and underwent eosin staining by immersing them in the staining solution for 5 min. A water rinse was performed on the samples before each solution change. Before immunostaining, slices were subjected to antigen retrieval using citrate buffer and incubated for 30 min with a BSA solution. Anti-CD68 Rabbit pAb (1:200) served as the primary antibody, and Cy3 conjugated Goat Anti-Rabbit IgG (H+L) (1:300) was used as the secondary antibody. DAPI was employed to stain the nucleus of all cells. Each group consisted of three rats. The slices were observed under fluorescence microscopy (Olympus BX51).

Statistical Analysis: The particle size distribution of magnetic Fe_3O_4 and NdFeB was presented as the mean ± SD of the total Fe_3O_4 and NdFeB particle sizes in TEM and SEM images. The sample number for statistical size distribution in both magnetic particles was 200.

Supporting Information

Supporting Information is available from the Wiley Online Library or from the author.

Acknowledgements

This work was supported by Ministry of Science and Technology of the People's Republic of China (2022YFA1203001, 2022YFA1203002), NSFC (T2321003, 22335003, 52222310, 22205039), STCSM (20JC1414902, 21511104900), and CPSF (2022M710733).

Conflict of Interest

The authors declare no conflicts of interest.

Data Availability Statement

The data that support the findings of this study are available from the corresponding author upon reasonable request.

Keywords

magnetically actuated, micro-batteries, swimmable, targeted power delivery, zinc ion batteries

Received: October 5, 2023
Revised: November 2, 2023
Published online: November 20, 2023

[1] J. Ma, R. Quhe, W. Zhang, Y. Yan, H. Tang, Z. Qu, Y. Cheng, O. G. Schmidt, M. Zhu, *Small* **2023**, *19*, 2300230.
[2] A. Libanori, G. Chen, X. Zhao, Y. Zhou, J. Chen, *Nat. Electron.* **2022**, *5*, 142.
[3] P. Zhang, F. Wang, M. Yu, X. Zhuang, X. Feng, *Chem. Soc. Rev.* **2018**, *47*, 7426.
[4] P. Li, M. Liao, J. Li, L. Ye, X. Cheng, B. Wang, H. Peng, *Small Struct.* **2022**, *3*, 2200058.
[5] Q. Xia, F. Zan, Q. Zhang, W. Liu, Q. Li, Y. He, J. Hua, J. Liu, J. Xu, J. Wang, C. Wu, H. Xia, *Adv. Mater.* **2023**, *35*, 2200538.
[6] W. Wang, C. Li, S. Liu, J. Zhang, D. Zhang, J. Du, Q. Zhang, Y. Yao, *Adv. Energy Mater.* **2023**, *13*, 2300250.
[7] D. Chao, W. Zhou, F. Xie, C. Ye, H. Li, M. Jaroniec, S. Z. Qiao, *Sci. Adv.* **2020**, *6*, aba4098.
[8] S. Lei, Z. Liu, C. Liu, J. Li, B. Lu, S. Liang, J. Zhou, *Energy Environ. Sci.* **2022**, *15*, 4911.
[9] M. Liao, C. Wang, Y. Hong, Y. Zhang, X. Cheng, H. Sun, X. Huang, L. Ye, J. Wu, X. Shi, X. Kang, X. Zhou, J. Wang, P. Li, X. Sun, P. Chen, B. Wang, Y. Wang, Y. Xia, Y. Cheng, H. Peng, *Nat. Nanotechnol.* **2022**, *17*, 372.
[10] L. Yuan, J. Hao, B. Johannessen, C. Ye, F. Yang, C. Wu, S.-X. Dou, H.-K. Liu, S.-Z. Qiao, *eScience* **2023**, *3*, 100096.
[11] M. Mimee, P. Nadeau, A. Hayward, S. Carim, S. Flanagan, L. Jerger, J. Collins, S. Mcdonnell, R. Swartwout, R. J. Citorik, V. Bulovic, R. Langer, G. Traverso, A. P. Chandrakasan, T. K. Lu, *Science* **2018**, *360*, 915.
[12] J. H. Lee, T.-M. Jang, J.-W. Shin, B. H. Lim, K. Rajaram, W. B. Han, G.-J. Ko, S. M. Yang, S. Han, D.-J. Kim, H. Kang, J. H. Lim, K.-S. Lee, E. Park, S.-W. Hwang, *ACS Nano* **2023**, *17*, 8511.
[13] A. D. Mickle, S. M. Won, K. N. Noh, J. Yoon, K. W. Meacham, Y. Xue, L. A. Mcilvried, B. A. Copits, V. K. Samineni, K. E. Crawford, D. H. Kim, P. Srivastava, B. H. Kim, S. Min, Y. Shiuan, Y. Yun, M. A. Payne, J. Zhang, H. Jang, Y. Li, H. H. Lai, Y. Huang, S.-I. Park, R. W. Gereau, J. A. Rogers, *Nature* **2019**, *565*, 361.
[14] X. Huang, D. Wang, Z. Yuan, W. Xie, Y. Wu, R. Li, Y. Zhao, D. Luo, L. Cen, B. Chen, H. Wu, H. Xu, X. Sheng, M. Zhang, L. Zhao, L. Yin, *Small* **2018**, *14*, 1800994.
[15] A. J. Bandodkar, S. P. Lee, I. Huang, W. Li, S. Wang, C.-J. Su, W. J. Jeang, T. Hang, S. Mehta, N. Nyberg, P. Gutruf, J. Choi, J. Koo, J. T. Reeder, R. Tseng, R. Ghaffari, J. A. Rogers, *Nat. Electron.* **2020**, *3*, 554.
[16] T. Takamatsu, Y. Sijie, F. Shujie, L. Xiaohan, T. Miyake, *Adv. Funct. Mater.* **2020**, *30*, 1906225.
[17] J. Ma, S. Zheng, L. Chi, Y. Liu, Y. Zhang, K. Wang, Z.-S. Wu, *Adv. Mater.* **2022**, *34*, 2205569.
[18] X. Shi, S. Pei, F. Zhou, W. Ren, H.-M. Cheng, Z.-S. Wu, X. Bao, *Energy Environ. Sci.* **2019**, *12*, 1534.
[19] X. Jin, L. Song, C. Dai, Y. Xiao, Y. Han, X. Li, Y. Wang, J. Zhang, Y. Zhao, Z. Zhang, N. Chen, L. Jiang, L. Qu, *Adv. Mater.* **2022**, *34*, 2109450.
[20] Y. Kim, X. Zhao, *Chem. Rev.* **2022**, *122*, 5317.
[21] Z. Qu, M. Zhu, Y. Yin, Y. Huang, H. Tang, J. Ge, Y. Li, D. D. Karnaushenko, D. Karnaushenko, O. G. Schmidt, *Adv. Energy Mater.* **2022**, *12*, 2200714.
[22] Y. Kim, G. A. Parada, S. Liu, X. Zhao, *Sci. Rob.* **2019**, *4*, aax7329.
[23] S. Yi, L. Wang, Z. Chen, J. Wang, X. Song, P. Liu, Y. Zhang, Q. Luo, L. Peng, Z. Wu, C. F. Guo, L. Jiang, *Nat. Commun.* **2022**, *13*, 4177.
[24] L. Liu, J. Wu, B. Chen, J. Gao, T. Li, Y. Ye, H. Tian, S. Wang, F. Wang, J. Jiang, J. Ou, F. Tong, F. Peng, Y. Tu, *ACS Nano* **2022**, *16*, 6515.

[25] J. Wang, M. Liao, X. Huang, P. Li, J. Li, L. Ye, Y. Gao, H. Peng, B. Wang, *J. Mater. Chem. A* **2022**, *10*, 10201.
[26] H. Ge, X. Feng, D. Liu, Y. Zhang, *Nano Res. Energy* **2023**, *2*, 9120039.
[27] S. Zheng, H. Wang, P. Das, Y. Zhang, Y. Cao, J. Ma, S. (F). Liu, Z.-S. Wu, *Adv. Mater.* **2021**, *33*, 2005449.
[28] X. Wang, S. Zheng, F. Zhou, J. Qin, X. Shi, S. Wang, C. Sun, X. Bao, Z.-S. Wu, *Natl. Sci. Rev.* **2019**, *7*, 64.
[29] X. Shi, Z.-S. Wu, J. Qin, S. Zheng, S. Wang, F. Zhou, C. Sun, X. Bao, *Adv. Mater.* **2017**, *29*, 1703034.
[30] C. M. Costa, R. Gonçalves, S. L. Méndez, *Energy Storage Mater.* **2020**, *28*, 216.
[31] D. Feng, Y. Jiao, P. Wu, *Angew. Chem., Int. Ed.* **2023**, *62*, 202215060.
[32] P. Li, M. Liao, S. Cui, J. Li, L. Ye, Y. Yang, C. Wang, B. Wang, H. Peng, *Angew. Chem., Int. Ed.* **2023**, *62*, 202300705.
[33] S.-W. Song, K.-C. Lee, H.-Y. Park, *J. Power Sources* **2016**, *328*, 311.
[34] H. Ning, J. H. Pikul, R. Zhang, X. Li, S. Xu, J. Wang, J. A. Rogers, W. P. King, P. V. Braun, *Proc. Natl. Acad. Sci. U. S. A.* **2015**, *112*, 6573.
[35] G. Sun, X. Jin, H. Yang, J. Gao, L. Qu, *J. Mater. Chem. A* **2018**, *6*, 10926.
[36] M. Zhu, Z. Wang, H. Li, Y. Xiong, Z. Liu, Z. Tang, Y. Huang, A. L. Rogach, C. Zhi, *Energy Environ. Sci.* **2018**, *11*, 2414.
[37] H. Lee, S. Kim, K.-B. Kim, J.-W. Choi, *Nano Energy* **2018**, *53*, 225.
[38] L. He, T. Hong, X. Hong, X. Liao, Y. Chen, W. Zhang, H. Liu, W. Luo, L. Mai, *Energy Technol.* **2019**, *7*, 1900144.
[39] S. Bi, F. Wan, S. Huang, X. Wang, Z. Niu, *ChemElectroChem* **2019**, *6*, 3933.
[40] M. Yu, Y. Peng, X. Wang, F. Ran, *Adv. Funct. Mater.* **2023**, *33*, 2301877.
[41] R. Sheng, J. Liu, W. Zhang, Y. Luo, Z. Chen, J. Chi, Q. Mo, M. Wang, Y. Sun, C. Liu, Y. Zhang, Y. Zhu, B. Kuang, C. Yan, H. Liu, L. J. Backman, J. Chen, *Adv. Sci.* **2023**, *10*, 2206814.
[42] W. Zhu, J. Mei, X. Zhang, J. Zhou, D. Xu, Z. Su, S. Fang, J. Wang, X. Zhang, C. Zhu, *Adv. Mater.* **2022**, *34*, 2207961.
[43] S. J. Bauer, J. C. Doloff, *Nat. Biomed. Eng.* **2021**, *5*, 1407.
[44] X. Liu, Y. Yang, M. E. Inda, S. Lin, J. Wu, Y. Kim, X. Chen, D. Ma, T. K. Lu, X. Zhao, *Adv. Funct. Mater.* **2021**, *31*, 2010918.
[45] K. Chen, L. Yan, Y. Sheng, Y. Ma, L. Qu, Y. Zhao, *ACS Nano* **2022**, *16*, 15261.
[46] T. Wu, W. Dai, M. Ke, Q. Huang, L. Lu, *Adv. Sci.* **2021**, *8*, 2100774.
[47] S. M. Kim, H. J. Kim, H. J. Jung, J.-Y. Park, T. J. Seok, Y.-H. Choa, T. J. Park, S. W. Lee, *Adv. Funct. Mater.* **2019**, *29*, 1807760.
[48] S. Wang, J. Xu, W. Wang, G.-J. N. Wang, R. Rastak, F. Molina-Lopez, J. W. Chung, S. Niu, V. R. Feig, J. Lopez, T. Lei, S.-K. Kwon, Y. Kim, A. M. Foudeh, A. Ehrlich, A. Gasperini, Y. Yun, B. Murmann, J. B.-H. Tok, Z. Bao, *Nature* **2018**, *555*, 83.
[49] Z. Zhang, W. Wang, Y. Jiang, Y.-X. Wang, Y. Wu, J.-C. Lai, S. Niu, C. Xu, C.-C. Shih, C. Wang, H. Yan, L. Galuska, N. Prine, H.-C. Wu, D. Zhong, G. Chen, N. Matsuhisa, Y. Zheng, Z. Yu, Y. Wang, R. Dauskardt, X. Gu, J. B.-H. Tok, Z. Bao, *Nature* **2022**, *603*, 624.
[50] Y. Zhao, T. Mei, L. Ye, Y. Li, L. Wang, Y. Zhang, P. Chen, X. Sun, C. Wang, H. Peng, *J. Mater. Chem. A* **2021**, *9*, 1463.
[51] I. K. Ilic, V. Galli, L. Lamanna, P. Cataldi, L. Pasquale, V. F. Annese, A. Athanassiou, M. Caironi, *Adv. Mater.* **2023**, *35*, 2211400.
[52] M. Xiao, N. Li, S. Lv, *Chem. Eng. J.* **2020**, *394*, 125000.
[53] H. Pan, Y. Shao, P. Yan, Y. Cheng, K. S. Han, Z. Nie, C. Wang, J. Yang, X. Li, P. Bhattacharya, K. T. Mueller, J. Liu, *Nat. Energy* **2016**, *1*, 16039.
[54] S. Cui, D. Zhang, G. Zhang, Y. Gan, *J. Mater. Chem. A* **2022**, *10*, 25620.
[55] Y. Zeng, X. Zhang, Y. Meng, M. Yu, J. Yi, Y. Wu, X. Lu, Y. Tong, *Adv. Mater.* **2017**, *29*, 1700274.
[56] X. Wu, J. Feng, J. Deng, Z. Cui, L. Wang, S. Xie, C. Chen, C. Tang, Z. Han, H. Yu, X. Sun, H. Peng, *Sci. China Chem.* **2020**, *63*, 1281.
[57] H. Lu, J. Hu, L. Wang, J. Li, X. Ma, Z. Zhu, H. Li, Y. Zhao, Y. Li, J. Zhao, B. Xu, *Adv. Funct. Mater.* **2022**, *32*, 2112540.